PAPER • OPEN ACCESS

Dissipated electrical power and electron density in an RF atmospheric pressure helium plasma jet

To cite this article: J Golda *et al* 2019 *Plasma Sources Sci. Technol.* **28** 095023

View the article online for updates and enhancements.

IOP ebooks™

Bringing you innovative digital publishing with leading voices to create your essential collection of books in STEM research.

Start exploring the collection - download the first chapter of every title for free.

Dissipated electrical power and electron density in an RF atmospheric pressure helium plasma jet

J Golda[1,2] , F Kogelheide[3], P Awakowicz[3] and V Schulz-von der Gathen[1]

[1] Experimental Physics II, Ruhr University Bochum, Germany
[2] Institute of Experimental and Applied Physics, Kiel University, Germany
[3] Institute for Electrical Engineering and Plasma Technology, Ruhr University Bochum, Germany

E-mail: judith.golda@rub.de

CrossMark

Abstract

Atmospheric pressure plasmas have great potential, especially for biomedical applications, due to the large number of reactive species produced. In particular with regard to these applications, the comparability of processes through appropriate control of plasma parameters is essential for treatment safety. Here we present a method for the *operando* determination of absolute absorbed power in an RF atmospheric pressure helium plasma discharge using miniaturized probes. A detailed error analysis demonstrates the reliability of the measured power values. With the help of a global model, the sheath width and electron density (4×10^{16}–$11 \times 10^{16}\,\mathrm{m}^{-3}$) are derived from these power measurements and compared to literature. The results and thus the validity of the electrical model are confirmed by a second, independent characterization method using optical emission spectroscopy and time-averaged imaging.

Keywords: atmospheric pressure plasma, COST-Jet, μ-APPJ, electron density, operando absorbed power, plasma impedance, helium plasma

1. Introduction

In the last 20 years, atmospheric pressure plasmas have gained increased attention due to their promising technological applications, especially in biomedicine. This has resulted in a considerable number of review papers and topical issues in leading scientific journals addressing the scientific challenges [1–5].

As compared to low-pressure plasmas, atmospheric-pressure plasmas can be designed relatively inexpensively and straightforward. Therefore, there is a wide variety of different jet sources used by several groups, for example in the field of biomedical applications [6–9]. Here, a significant influence of plasma treatment on biological materials could be demonstrated. However, these scientific results suffer from reliability problems: besides the large variance due to the

natural fluctuations of the treated biological substrates, the observed effects and underlying mechanisms were rarely traced back to the plasma processes. These plasma processes in turn depend strongly on the plasma source used. Thus, the isolation of individual influences of the plasma parameters is hampered, so that the promising results obtained are often not transferable.

In the meantime, this topic has also been discussed by the modeling community. With the help of verification and validation mechanisms based on different simulation codes or detailed uncertainty analyses, the topic of reproducibility and predictive power is also addressed [10].

Overall, reproducibility is not a problem that only plasma physicists are confronted with. Instead, it is a demanding challenge that science in general faces, especially in the life sciences [11]. Just recently, this aspect has again been the subject of numerous editorials and articles in high-ranking journals such as Nature [12, 13].

In atmospheric pressure plasma physics, the published electrical parameters of a discharge used in experiments have

often been based on generator power [14, 15]. Occasionally the ignition and arcing points were also given [16]. This practice has become established, although for both low-pressure and atmospheric-pressure plasmas the generator power is not a representative, meaningful parameter for the power absorbed in the plasma [17, 18], since the losses of the generator power strongly depend on the electrical circuit. Therefore, these data do not allow a transfer from one experimental setup to another.

An alternative parameter is the applied voltage across the discharge gap [19], which is closely related to the reduced electric field in the discharge. In principle, this control parameter is transferable. However, it does not cover the entire physically relevant information, especially if different chemical gas compositions are to be compared. For the same electric field, the plasma parameters strongly depend on the chemical composition of the operating gas. This is clearly illustrated by the example of plasmas generated from molecular gases, which require a significantly higher applied voltage than from noble gases in order to generate a comparable electron density. Jonkers *et al* introduced the concept of equi-operational plasmas for this purpose [20]. Based on the electron particle and energy balance it can be deduced that the set of characteristic size of the confining structure, power density and gas pressure is suitable to define the external experimental control parameters. In order to be able to implement this theoretical concept experimentally, we have decided to use the COST Reference Microplasma Jet as an example, which was developed within the framework of the COST Action MP1101 and proposed as a reference plasma source. Since the geometry and thus also the characteristic size of the discharge in the COST-Jet are fixed, only pressure and power density need to be determined when results are compared for this plasma source. Therefore, it is desirable to measure the absorbed power converted in the plasma and calculate the power density from it.

This paper presents the method for measuring the dissipated electrical power in the COST-Jet and its limitations. Absolute values of the dissipated power are calculated and a detailed error estimation is performed. Using an electrically equivalent model, the time-averaged sheath width and electron density can be derived from the electrical measurements. In order to verify the model, both electron density and sheath width and their dependence on the power absorbed in the plasma are compared with an independent optical emission spectroscopy method measuring the rotational and vibrational transitions of molecular nitrogen transitions and simple photographs of the discharge.

2. Experimental

2.1. Atmospheric pressure plasma jet

The atmospheric pressure plasma jet used in this study is the COST Reference Microplasma Jet (COST-Jet) [21] that was developed within the EU COST (European Cooperation in Science and Technology) action MP1101 'Biomedical
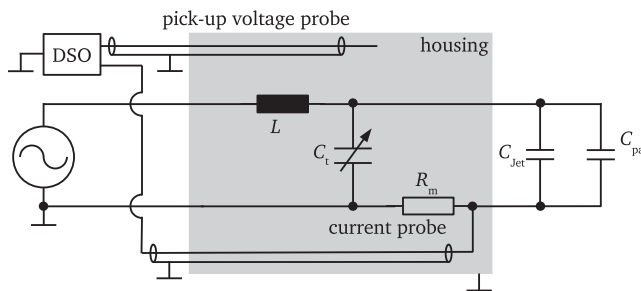
Figure 1. Simplified electrical setup of the COST-Jet configuration without plasma.

Applications of Atmospheric Pressure Plasma Technology'. The COST-Jet is usually operated using 13.56 MHz excitation and a helium feed gas. The plasma is generated between two plane-parallel electrodes, one of which is grounded and one of which is connected to the power supply via an LC resonance circuit. The electrodes are encapsulated by two quartz panes, thus forming the discharge channel with a cross section of 1×1 mm. The gas supply is controlled by mass flow controllers (Analyt-MTC series 358) and typical feed gas flow rates are between 0.25 and 2.00 slpm. Unless otherwise stated, a helium gas flow of 1000 sccm is used in this publication. To reduce humidity in the feed gas, a cold trap was used. The COST-Jet includes two internal, miniaturized, electrical probes that are implemented into a casing close to the electrodes. A simplified scheme of the electrical setup is shown in figure 1. The internal voltage probe consists of a pick-up antenna close to the powered electrode. The current probe is a current-sensing resistor. To measure voltage and current signals, these probes are connected to a $4 \, \mathrm{GS \, s^{-1}}$ oscilloscope (Agilent Technologies DSO7104B). To calibrate the internal voltage probe, a commercial voltage probe (Tektronix P5100A) is used. Shielding of the grounded electrode reduces the amount of measured reactive current and thus the influence of stray capacities [22]. For a more detailed description of the COST-Jet, see a previous publication [21].

2.2. Optical emission setup

Absolutely calibrated optical emission spectroscopy using a broadband echelle spectrometer (ESA-4000, LLA Instruments, Germany) with a spectral resolution of 0.015–0.06 nm in the wavelength range of 200–800 nm was carried out to analyze the electron density. The electron density was calculated using a collisional radiative model in combination with numerical simulation published by Bibinov *et al* which focuses on the nitrogen molecular bands [15, 23]. It is based on the ratio of the emission spectra of molecular nitrogen $N_2(C^3\Pi_u - B^3\Pi_g)$ and molecular nitrogen ion $N_2^+(B^2\Sigma_u^+ - X^2\Sigma_g^+)$. Therefore, a feed gas flow of 1000 sccm helium with an admixture of 0.1 sccm nitrogen as a tracer gas is used for these measurements.

To determine the averaged gas temperature, the measured spectra are fitted to spectra simulated for various gas temperatures and the rotational structure of the vibrational band of N_2(C-B,0-0) is compared. This holds true under the assumption that rotational and translational degrees of freedom of diatomic

molecules have equal temperatures at atmospheric pressure [15, 23–25].

In He–N$_2$ discharges under atmospheric pressure conditions, nitrogen molecular emission N$_2$(C-B) can be excited by electron impact excitation directly from the ground state of N$_2$(X), stepwise excitation via nitrogen metastable N$_2$(A) and energy-pooling reaction of two nitrogen metastables. N$_2^+$(B-X) emission can be generated by direct electron excitation of N$_2$(X) as well. Moreover, excitation of N$_2^+$(B-X) can further take place due to collisions of helium metastables with N$_2$(X) and stepwise excitation from the ground state of nitrogen ions, N$_2^+$(X) [25].

In order to obtain the electric field, *E*, the Boltzmann equation is solved in local approximation for different electric fields using the program code 'EEDF' by Napartovich *et al* for the defined used gas mixture [26]. Using the simulated electron velocity distribution function and the known cross section for electron impact excitation, it is possible to calculate the rate constants for electron impact excitation of N$_2$ for various electric fields. To calculate the electron density, the rate constant for electron impact excitation as a function of the electric field and the measured absolute intensity of the N$_2$(C-B,0-0) transition is taken into account [23–25].

All underlying assumptions and limitations to this method for discharges in He–N$_2$ admixtures are described in more detail in Pothiraja *et al* [25]. The collisional-radiative model is further explained in Offerhaus *et al* [23].

For photographs of the discharge, a digital reflex camera (Canon EOS 60D) and a 70 mm objective lens were used.

3. Results and discussions

3.1. Reproducibility of the power measurement

To use the dissipated power as an equi-operational parameter according to Jonkers *et al* [20] as an *operando* external control parameter, a measurement method based on miniaturized current and voltage probes integrated into the COST-Jet was developed. Thus, a comparison between plasma discharges under different experimental conditions, e.g. operated using different chemical feed gas compositions, can be performed. To interpret the significance of such comparisons, a detailed error analysis of the power measurement is required. In the following section, such a detailed error analysis is shown. All measured variables entering the calculation are analyzed. The core of the measurement method are the two electrical parameters measured by miniaturized probes, voltage across the discharge gap and current dissipated in the discharge. As already described in an earlier publication [21], the power dissipated in the discharge is calculated via

$$P = V_{rms} \cdot I_{rms} \cdot \cos\left(-\frac{\pi}{2} + \Delta\phi - \Delta\phi_{ref}\right)$$

$$= \frac{1}{2} \cdot c \cdot V_{0,int} \cdot \frac{R_m + R_t}{R_m R_t} \cdot I_{0,int} \tag{1}$$

$$\cdot \cos\left(-\frac{\pi}{2} + (\varphi_V - \varphi_{V,ref}) - (\varphi_I - \varphi_{I,ref})\right), \tag{2}$$

V_{rms} and I_{rms} denote the effective values of voltage and current, $\Delta\phi$ denotes the phase difference between current and voltage and $\Delta\phi_{ref}$ is the corresponding phase difference when the plasma is switched off. These quantities are in turn determined from the following quantities: $V_{0,int}$ and $I_{0,int}$ are the amplitudes of a sinusoidal curve which is fitted to the waveform measured by the internal voltage and current probe. *c* is a calibration factor that describes the proportionality between the voltage measured using the internal voltage probe and the actual voltage across the discharge gap. This calibration factor has to be determined once by comparison to a measurement using a commercial voltage probe. R_m is the measuring resistor and R_t the terminating resistor which is connected in parallel. φ_V and φ_I each describe the phase position of the measured voltage or current signal and $\Delta\phi_{ref} = \varphi_{V,ref} - \varphi_{I,ref}$ is the corresponding reference phase difference. $V_{0,int}$, $I_{0,int}$, φ_V and φ_I are measured quantities, whereas all other quantities are calibration quantities. All these quantities are error-prone and can cause a significant uncertainty in the determination of the dissipated power due to error propagation.

Here, the total error is calculated by summation over the absolute values of statistical and systematic error.

For the power measurements presented here, the statistical errors are caused by fluctuations of the measured signal shape, for example by the jitter of the measurement data, but also by electrical noise of the 8-bit analog-to-digital converter and the sample rate of the oscilloscope. Due to the small size of the plasma discharge, the expected dissipated power is small. Therefore, the expected phase differences to be measured are also small, so that this error has a particularly large influence on the total error of the power measurement. To reduce the aforementioned errors, the waveforms are averaged over 2048 measurements. For a sufficiently large time resolution of the RF period, the oscilloscope has a comparatively high sample rate of 4 GS s^{-1} to reduce the digitizing errors of the phase measurement. The voltage scale is selected according to the measured signal so that the full range of the analog-to-digital converter is used as far as possible, without requiring a change of scale during a measurement. In order to estimate the magnitude of the errors and their effects on the calculation of the power, each measurement was repeated 10 times under identical experimental conditions using the same discharge voltage and number of averages. The total statistical error was calculated using Gaussian error propagation, taking into account the statistical error of amplitude and phase of the signals measured with the voltage and current probes. For all measurements, the maximum statistical error was 1%. This is comparable to commercial power measurement systems such as the RF power sensor 'Octiv' from Impedans [27].

For the estimation of the systematic error, the uncertainties of the three calibration parameters were considered in this study:

    (i) The calibration factor *c* is sensitive to errors of the internal voltage probe during the calibration procedure as described in [21]. First, the calibration factor depends

on the compensation of the commercial voltage probe for the input capacitance of the oscilloscope. This process, in turn, is strongly dependent on the performing experimenter, which can have a corresponding effect on the calibration factor. In order to minimize this error, the probe was always attached to the same oscilloscope channel. Thus, the internal voltage probe only needs to be calibrated once and errors due to differences between the channels or by compensation are avoided. Second, the measured voltage depends strongly on the position of the pick-up antenna of the internal voltage probe. If this position is changed, for example due to an accidental displacement during handling, the measured voltage also changes. This change can be estimated using a first approximation: the electric field around a wire can be described by $\vec{E} = \lambda/(2\pi\epsilon_0\epsilon_r r) \cdot \vec{e}_r$ with λ being the linear charge density. The magnitude of the electric field strength and thus also the induced measured voltage depends antiproportionally on the radial distance r between the pick-up antenna and the copper conductor. A small change in the position and thus in the distance r is translated into a corresponding change in the electric field strength. For example, a change in distance of 0.05 mm from the original position at an original distance of 2 mm from the conductor causes a change in the measured voltage of 2.5%. This results in an absolute calibration factor error of about $\delta c = 50$, where c depends on the device and usually is in the range from 1900 to 2700.

(ii) The deviation of the resistances R_t and R_m required for the calculation of the current is given by the manufacturers as guaranteed less than $\delta R_t = 2\%$ and $\delta R_m = 1\%$.

(iii) The reference phase errors are firstly influenced by the jitter of the signal during the reference measurement. Second, physical changes in the reference phase difference during this measurement can cause systematic errors. These changes can be caused by changes in the electrode surface, parasitic capacitance, or excessive heating of the coil, which introduces a considerable amount of resistive impedance into the electrical circuit. Therefore, this error is considered with $\delta\varphi_{ref} = 0.002$ rad, whereby the reference phase typically has an amount of $\Delta\phi_{ref} = 0.07$ rad. This value was determined by a day-to-day analysis with a sample size of $n = 4$.

In addition, there are some more general sources of error that can influence the measurements. However, these are considered to be negligible for the power calculations, as preventive measures have been taken. A deviation of the measured signals from the assumed sinusoidal shape causes an error, but was found to be neglectable by examining the signals for higher harmonics using a Fourier-transform analysis. In addition, the position of the electrode shielding has an influence on the current measurement: if the position is changed, the proportion of the measured displacement current increases. This overestimates the measured current, because due to the comparatively large error in the measurement of the
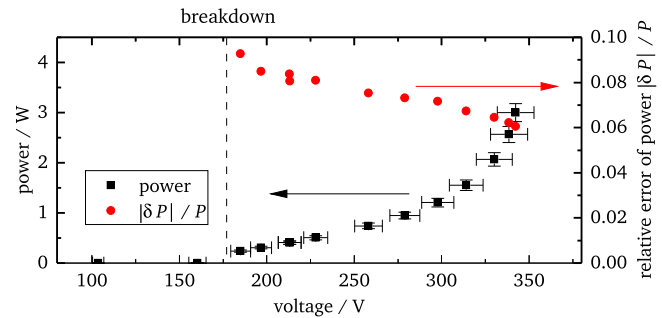

Figure 2. Calculated dissipated plasma power with respective error bars (■) and relative error (●) for a discharge operated with a typical gas flow rate of 1000 sccm helium and with an admixture of 5 sccm oxygen. Reprinted with permission [28].

phase difference, this change may not be adequately compensated. Parasitic capacitances or the introduction of the commercial voltage probe into the electrical circuit change the power coupled into the plasma. During the calibration procedure, the housing of the COST-Jet was therefore closed to shield the LC resonant circuit. Signals reflected at the oscilloscope input can cause standing waves in the probe cables, but should be minimized by the 50 Ω termination. Other effects such as bad contacts (e.g. solder joints) can also cause comparable wave reflections and thus change the measured signal. Ground loops can cause false reference potentials for voltage measurements. Therefore, all connections have been kept as short as possible. Finally, an important challenge when working with RF excitation is the cross-talk between electrical lines, such as those of probes. This crosstalk is avoided by carefully shielding the cables even inside the housing.

To illustrate the overall impact of these errors, the results for a typical measurement of dissipated power are discussed below. Figure 2 shows the dissipated power in a plasma discharge operating at a gas flow rate of 1000 sccm helium with an admixture of 5 sccm oxygen. The dissipated power (■) and the absolute error of the power (see error bar) increase with increasing voltage. In contrast, the relative error (●) decreases with increasing voltage. The maximum relative error of the determined power is 9.3% and the average relative error over the entire voltage range is 7.5%. Remarkably, the error of the measured voltage appears to be greater than that of the power. However, this impression is only caused by the scaling and aspect ratio of the scales.

Compared to the commercial power measurement system 'Octiv' mentioned above, this error seems relatively large. However, the error of this commercial system also increases with the phase angle of the load impedance. For the phase angle of the plasma impedance in the COST-Jet (about $-80°$), the power measurement error according to the data sheet is thus more than 10 percent. In addition, this system is not specified for measured powers below 200 mW. A further disadvantage of commercial systems is the mounting of the probe in the supply cable, so that an error of unknown size is introduced into the measurement if power is deposited between the probe and plasma in the cable.
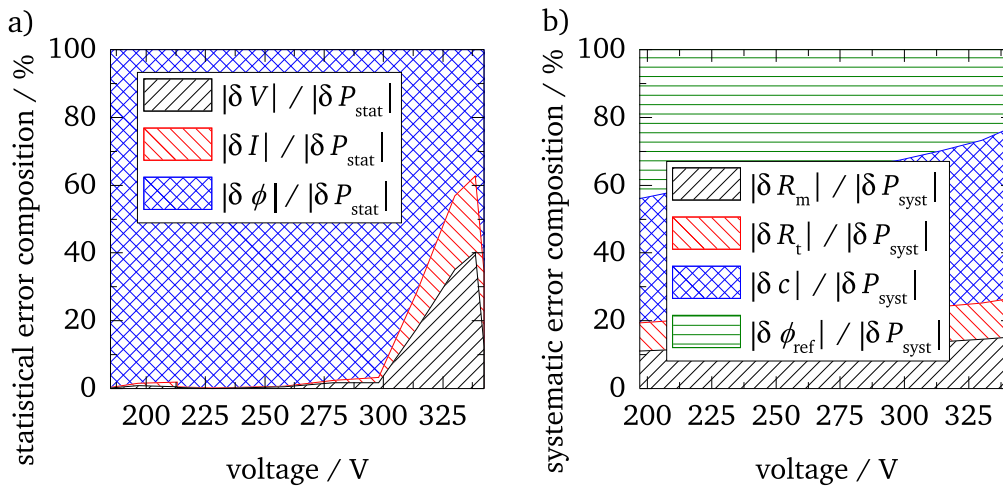
Figure 3. Composition of (a) statistical and (b) systematic error. The statistical error is caused by fluctuations in voltage U, current I and phase difference ϕ. The systematic error consists of measuring R_{m} and termination resistor R_{t}, voltage calibration factor c and the reference phase difference ϕ_{ref}. Reprinted with permission [28].

To analyze the origin of these errors, figure 3 shows the composition of the two components of the total error: (a) the statistical error and (b) the systematic error. The statistical error is mainly caused by the phase measurement. With higher voltage, current and voltage errors increase over-proportionally, since the reference phase error, unlike current and voltage errors, does not depend on the signal amplitude, but remains constant once the reference phase difference has been determined. The large phase error at the highest measured voltage is caused by the fact that the discharge is close to the transition to constricted mode. Therefore, phase instabilities are not unlikely. For all data points, the statistical error is less than 6% of the total error and therefore negligibly small.

The systematic error is composed of the errors of the resistors, the calibration error and the reference phase error. At low voltages, the error is mainly caused by the reference phase error. This is followed by the calibration error and the resistance error. This ratio changes with increasing voltage. While the error portion caused by the resistors remains approximately constant, the portion of the calibration error increases as the reference phase error decreases. This behavior is caused by the influence of the reference phase error, which does not depend linearly but via a tangent function on the increasing power (compare derivative of equation (1)).

In order to illustrate the relevance of the overall error to the significance of measurements, three scenarios are considered:

1. An identical setup in the same laboratory.
2. Different COST-Jet setups in the same laboratory.
3. Different COST-Jet setups in different laboratories.

Scenario (i) applies if the dissipated power is measured with a single COST-Jet setup in the same laboratory (i.e. with the same oscilloscope, the same commercial voltage probe, etc). If the calibration is performed only once and then used consistently, only the reference phase error and the statistical error are relevant for the comparison of these measurements.

This results in an effective reduction of the relative error for power to $\delta P/P = \pm 4.6\%$. This scenario is, for example, relevant for the comparison of the data in this publication.

Scenario (ii) applies when the dissipated power of different COST-Jet assemblies is measured in the same laboratory. If the calibration was performed once per setup, the relative error according to the calculations in the previous chapter is $\delta P/P = 9.3\%$. This scenario applies to the comparison of results on different assemblies.

Scenario (iii) applies if the dissipated power is measured using different COST-Jet assemblies in different laboratories. This includes the use of different instruments, i.e. a commercial voltage probe for the calibration of the internal voltage probe. This scenario applies when researchers from different laboratories compare their results from experiments with different COST-Jet assemblies. Here, the accuracy of the measurements can be reduced due to the systematic errors of the laboratory equipment, e.g. the commercial voltage probe, but also due to different experimenters, e.g. executing the compensation procedure of the commercial voltage probe.

In summary, the power measurement is an adequate control parameter for the comparison of atmospheric pressure plasmas operated with different gases. Despite the challenges posed by the capacitive character and small dimensions of the plasma, an *operando* power measurement could be realized by careful probe design and evaluation of the current and voltage signals. A detailed error estimation allows conclusions to be drawn about the significance and transferability of research results. In principle, the power measurements can be perceived as reproducible within the defined error limits. The error of the three scenarios presented here must be taken into account when comparing the significance of results. Thanks to the special design of the COST-jet discharge, results from different laboratories can now be compared. Furthermore, all error bars are in the same order of magnitude as discussed for scenario 1. They are therefore omitted for better readability.
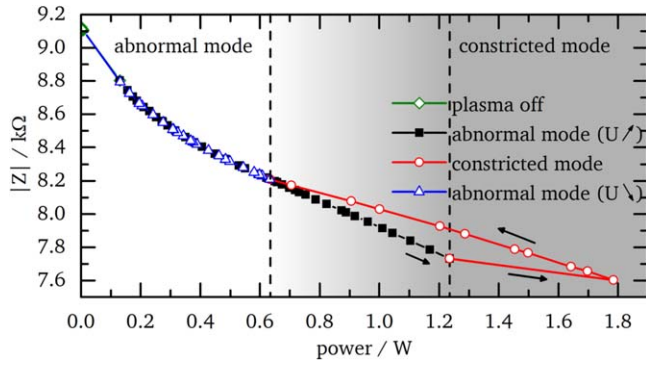
Figure 4. Measured impedance of helium discharge as a function of the dissipated power (atmospheric pressure, gas flow rate 1000 sccm).

3.2. Electrical model

Not only can the actual power dissipated in the plasma be calculated from the voltage, current and phase measurement, by making assumptions about the electrical character of the discharge, intrinsic plasma parameters such as plasma impedance, resistance and reactance can be calculated [29, 30]. This allows the estimation of the time-averaged sheath width and the corresponding electron density in a microdischarge. Because the measurement method described above provides reliable and reproducible values for the dissipated power, it can now be used to perform robust calculations.

The magnitude of the impedance $Z = R + iX$ can be calculated by dividing the measured voltage amplitude V by the current amplitude I. To obtain the resistance R (real part) and the reactance X (imaginary part) for a sinusoidal signal form, this value must be multiplied by the cosine or sine of the phase difference:

$$|Z| = \frac{V}{I} \tag{3}$$

$$R = \frac{V}{I}\cos(\Delta\phi) \tag{4}$$

$$X = \frac{V}{I}\sin(\Delta\phi). \tag{5}$$

Figure 4 shows how the magnitude of the plasma impedance $|Z|$ depends on the power dissipated in the discharge for a gas flow rate of 1000 sccm pure helium at atmospheric pressure. The impedance measurements were carried out by increasing the generator power from plasma off ($\diamond$) until the discharge is ignited. After the ignition, the discharge is in the state of homogeneous glow discharge mode. It directly covers the whole electrode area (abnormal glow discharge mode) without any sign of spreading along the electrode area with increasing voltage (normal glow discharge mode). If the generator power was further increased the homogeneous discharge in abnormal mode (■) was transformed into the so-called constricted mode ($\circ$), a bright filament at the tip of the electrodes. Subsequently, the generator power was reduced again. Here, the plasma discharges shows a hysteresis when switching back to abnormal mode as marked by two dashed lines. The arrows indicate the temporal evolution, straight
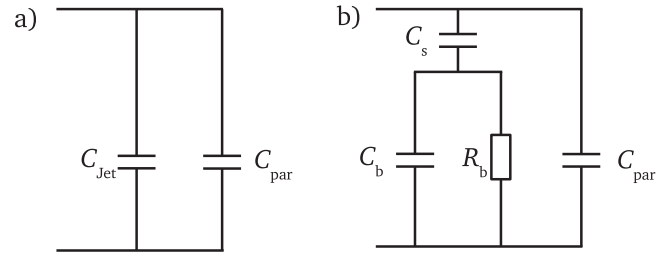

Figure 5. Equivalent electrical circuit used for the calculations: (a) plasma off and (b) plasma on.

lines connect the data points to guide the eye. In addition, the constricted mode is colored gray.

The impedance is maximum if the plasma discharge is not yet ignited. In abnormal mode, the plasma impedance decreases monotonously with increasing power. At low powers the impedance decreases steeper than at high powers. In constricted mode, the impedance decreases even further. The observed behavior of plasma impedance seems reasonable and is comparable to the impedance measurements on atmospheric pressure discharges of Zhu *et al* [31] and Overzet *et al* [32], who measured an atmospheric pressure RF helium plasma jet and a DC hollow cathode helium discharge, respectively.

The amount of impedance determined here is notable. When the plasma is not ignited yet, the absolute value of the impedance is about 9 kΩ. In this situation, the impedance should be purely imaginary and correspond to the capacitance of a parallel plate capacitor with the dimensions of the COST-Jet. The plasma-off impedance corresponds to a value of $C = (\omega X_p)^{-1} = 1.3$ pF, but the capacitance of the COST-Jet is only about $C_{Jet} = 0.3$ pF. This deviation of more than 300% is caused by additional parasitic capacitances, e.g. by the housing. As the electrode shielding (see section 2.1) reduces stray capacitances due to floating objects in the vicinity of the jet, this parasitic capacitance is constant and can be easily corrected for. It was taken into account in the equivalent circuit by an additional constant capacitance parallel to the COST-Jet (see figure 5(a)). This correction only affects the absolute value of the impedance, the shape remains unchanged. The measurement of the dissipated power is also unaffected, since no power is consumed in the parasitic capacitance. Considering the parasitic capacitance ($C_{par} = C - C_{Jet} = 1.0$ pF), the corrected plasma impedance can be determined from the measured impedance, which is of the order of $Z_p = 40$ kΩ. This value corresponds very well with the aforementioned measurements by Overzet *et al* [32] and simulations of an atmospheric pressure helium RF plasma by McKay *et al* [33].

For a physical interpretation of the impedance, the resistive and reactive components are considered separately. Figure 6(a) shows the resistance of the helium discharge as a function of the dissipated power. Since bulk resistance is associated with electron density [34], a decrease of resistance in abnormal mode would be expected with increasing dissipated power. Surprisingly, we observe the opposite, namely that the resistance in the helium discharge increases with increasing power. This observation confirms measurements
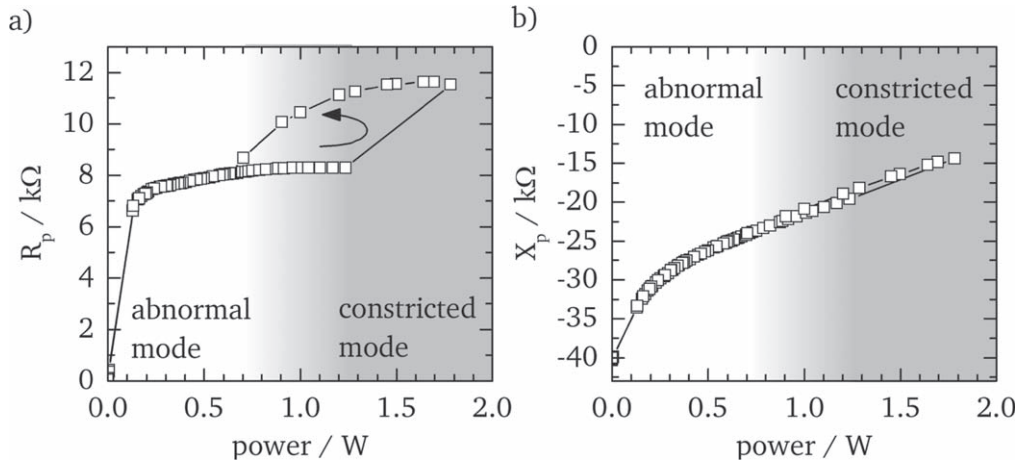
Figure 6. (a) Plasma resistance and (b) reactance of helium discharge as a function of the dissipated power (atmospheric pressure, gas flow rate 1000 sccm).

by Marinov and Braithwaite [35] who found the same trend at a similar discharge and attributed it to dissipation of power in the sheaths. The constricted mode manifests itself through discontinuity and resistance increases sharply. We explain this behavior with a slightly increased electron density in the filament while the electron density outside the filament in the co-existing homogeneous mode is greatly reduced compared to the prior homogeneous discharge. The decreased specific resistance of the filament exhibiting a very small cross-sectional area cannot outweigh the increased specific resistance in the co-existing homogeneous glow exhibiting a cross-sectional area almost equal to the electrode surface. This assumption is based on measurements of Schröder *et al* and Spiekermeier *et al* [36, 37]. However, any interpretation of global measurements such as electrical characteristics to explain local phenomena such as this filament involves a degree of uncertainty. Figure 6(b) shows the reactance as a function of the dissipated power. The comparison with figure 4 clearly shows that the amount of impedance is dominated by the reactance of the discharge, which underlines the capacitive character of the discharge.

The decrease of the absolute reactance in abnormal mode can be caused by an increase of the sheath capacity, i.e. a decrease of the sheath width. In constricted mode, the reactance of the discharge is even further reduced. Again, this behavior has to be interpreted with caution due to the spatial confinement of the filament. In the following, we will therefore limit the discussion to the abnormal discharge mode.

For a detailed analysis and interpretation of the processes it is necessary to isolate the influence of the bulk plasma and the sheaths. For this purpose, an equivalent electrical circuit is used which is adapted to the characteristics of the discharge and reflects the different zones, i.e. sheath and bulk. The model used in this publication is based on the so-called homogeneous model by Lieberman *et al* [38, 39]. This is a highly simplified model that does not take into account sheath effects such as stochastic heating (sheath resistance) or ion heating (current source).

Figure 5 shows the equivalent circuit for the plasma before ignition (a) and after ignition (b). A capacitively coupled atmospheric pressure plasma can be represented by a circuit of a sheath capacitance C_s in series with a parallel circuit of bulk capacitance C_b and bulk resistance R_b. Since for collisional plasmas the collision frequency is much higher than the excitation frequency ($\nu_m \gg \omega$), the inductance, which usually reflects the electron inertia, can be omitted [33].

The plasma impedance ($Z_p = R_p + iX_p$) can be related to the components of the equivalent electrical circuit (X_s, X_b, and R_b) by solving the equation system resulting from figure 5(b) [33]:

$$X_s = X_p + \frac{R_p^2}{X_p - X_0} \tag{6}$$

$$X_b = X_0 - X_s \tag{7}$$

$$R_b = R_p\left[1 + \frac{R_p^2}{(X_p - X_0)^2}\right]. \tag{8}$$

X_0 represents the capacitance of the discharge gap without plasma $X_0 = (\omega C_{Jet})^{-1}$. Equations (6)–(8) can be used to determine the size of the equivalent electrical components from the plasma impedance.

Figure 7 shows the bulk resistance of a helium plasma determined from the measured impedance using the electrical model described above as a function of the dissipated power. As long as the plasma is not ignited, the dissipated power is 0 W. Since in this case there are no free charge carriers between the two electrodes, there is no conduction current and no plasma bulk. Therefore, the bulk plasma resistance corresponds to 0 Ω and the sheath capacitance X_s is equal to the capacitance of the discharge gap X_0.

In abnormal mode the plasma bulk resistance now decreases as expected with increasing dissipated power. As the plasma already fills the full discharge gap, it cannot expand further with a current increase and reacts by adjusting the plasma properties. The higher the power, the higher the electron density and the lower the electrical resistance. At the
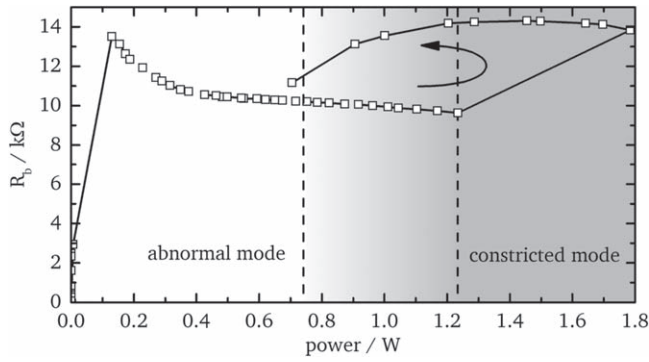
Figure 7. Bulk resistance as a function of dissipated power for helium (atmospheric pressure, gas flow rate 1000 sccm).

Figure 8. Bulk and sheath width in the abnormal mode deduced from the electrical impedance (■) and optical measurements (□) as a function of the dissipated power for helium discharge. The dashed line marks modeling results from Waskoenig [40].

transition to constricted mode, the resistance increases surprisingly. Usually, the electron density should be higher than in abnormal mode and the resistance should therefore decrease. By concentrating the discharge in constricted mode on a small area of about $1\,mm^2$ at the tip of the electrodes, the increasing number of electrons is compensated by the reduction of the area. Therefore, despite the smaller specific resistance, the total resistance increases. In addition, in constricted mode the waveforms of current and voltage deviate slightly from the sinusoidal waveforms, so that the calculation of the power must be considered with caution.

In summary, the analysis of the discharge impedance revealed an additional parasitic capacitance to be considered in the calculations. Using the homogeneous model as an equivalent circuit, the contradiction between the expected and measured resistance of the helium plasma, which was also observed by Marinov and Braithwaite, could be resolved. The dependence of the plasma resistance is caused by the ratio between sheath and bulk impedance $R_p = R_b \left/ \left(1 + \left(\frac{R_b}{X_0 - X_s} \right)^2 \right) \right.$. The interaction of these parameters, electron density and sheath properties, is analyzed in more detail below. From the isolated sheath and bulk components X_s and R_b further plasma parameters can be derived.

3.2.1. Sheath width. The plasma sheath in front of the electrodes plays a decisive role for the stability of the discharge in atmospheric pressure plasmas due to their large surface-to-volume ratio. If the sheath width approaches half of the discharge gap, the quasi-neutral bulk is suppressed and the plasma discharge can collapse. Therefore, the properties of the sheath are investigated in the following. The time-averaged sheath width s_0 can be calculated from the sheath capacity X_s by assuming a series combination of two nonlinear sheath capacitances using the following formula [38]

$$s_0 = \omega \epsilon_0 A X_s / 2. \qquad (9)$$

This formula is only valid in abnormal mode, since the cross-sectional area of the discharge A, which is included in the calculation, changes drastically in constricted mode. Figure 8 shows the time-averaged sheath width s_0 as a function of the dissipated power. In abnormal mode the average sheath width
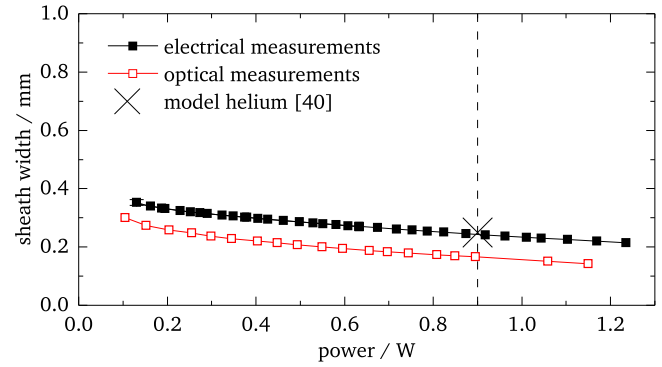
varies between 350 and 210 μm. Thus, its expansion for all dissipated powers considered is always less than half of the electrode gap (500 μm). With increasing dissipated power, the sheath width decreases monotonously, while the bulk width $b_0 = l - 2s_0$ increases accordingly. This behavior is initially unexpected and in contrast to low-pressure discharges. In typical capacitively coupled sheath models, the sheath also increases with increasing applied voltage [41]. For atmospheric pressure helium plasmas, however, a decrease has been observed by several authors both experimentally [42–44] and in simulations [45]. One explanation is the small change of the electron temperature with the dissipated power and the independence of the electrical permittivity of the plasma from the dissipated power [46].

Schaper *et al* also observed in experiments with phase-resolved optical emission spectroscopy and in modeling results a decreasing sheath width with increasing dissipated power [47]. The determined sheath width also agrees well with a 1D hybrid model for the coplanar μ-APPJ operated in helium by Waskoenig [40]. At a power density of $3\,W\,cm^{-2}$ in the simulation, which corresponds to a dissipated power of 0.9 W in the COST-Jet geometry with an electrode area of $30\,mm^2$ (marked by a dashed line in figure 8), an RF-averaged sheath width of about 250 μm (cross in figure 8) results. This is in good agreement with the impedance measurement, which reveals a sheath width of 245 μm.

Considering the simplicity of the model used here, this agreement is remarkably good. Nevertheless, the results should be evaluated with caution, as the absolute value of the sheath width depends strongly on the sheath model used. Depending on this, equation (9) and thus the sheath width can be modified by multiplication with sheath model dependent factors. Equation (9) represents a neutral approach (factor 1.0). However, the factor 0.76 [48] was also proposed for collisional sheaths in low-pressure plasmas, resulting in a sheath width of 150 μm. Nevertheless, the relative trend also agrees very well with the aforementioned studies.

The displayed error bar in figure 8 for the first data point represents the largest statistical error in the measurement which was 4.0%. The systematic errors are between 29% and 150% for the sheath thickness. This error may seem large at
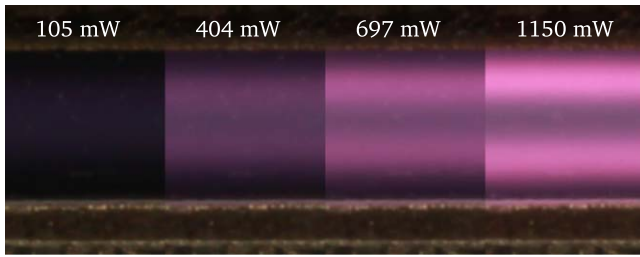
Figure 9. Segmented photograph of the emission intensity of a helium discharge between the plane-parallel electrodes (top/bottom) at 105 mW, 404 mW, 697 mW and 1150 mW, respectively. All photographs were taken using the same exposure time, aperture and ISO value.

Figure 10. Normalized intensity profiles of the helium discharge at dissipated powers of 105, 549 and 1150 mW.

first, but it is comparable with errors of other plasma diagnostic measurement methods. In addition, a systematic error has no influence on the trend of the measured data, since systematic errors act in the same direction for all measurements and thus only absolutely shift the curve. However, the additional comparison with the simulation results of [40] indicates a fundamental overestimation of the systematic error.

To further support the results from the global model, the sheath width was therefore additionally determined from optical images. For this purpose, a photo of the optical appearance of the plasma discharge was taken at various dissipated powers. Subsequently, intensity profiles were created from the images and the sheath width was evaluated.

Figure 9 shows a segmented image of the plasma channel at different power values. The driven and grounded electrode are shown in gray at the top and bottom, respectively. Between these electrodes, the helium plasma is located, which has a light purple coloration on the images. Overall, the intensity of the emission increases with increasing power. The images show that at low dissipated powers (105 mW) the emission is particularly present in the bulk part of the discharge. When the power is increased, the emission shifts towards the electrodes. Pronounced emission zones at the edges of the sheaths are formed. These have already been observed in several experimental and numerical studies [40, 47, 49, 50] and are due to the increased emission of secondary electrons and electrons created in the sheath area by, for example, Penning ionization and pooling reactions.

Several designations are used in the literature for these two different emission structures. As the emission structure of the discharge at low powers is similar to the classic α-mode of low-pressure discharges, the term α-mode has also become established. Since the physical mechanism of action is different, however, Hemke *et al* have also introduced the name Ω-mode [51]. Also for the sheath structures at higher powers the name γ-like mode exists in the literature analogous to the low pressure pendant. However, since this is caused less by the classical secondary electrons released at the electrode than by electrons produced in the sheath by Penning and pooling reactions and then accelerated, Bischoff *et al* and Gibson *et al* also use the term Penning mode [52, 53].
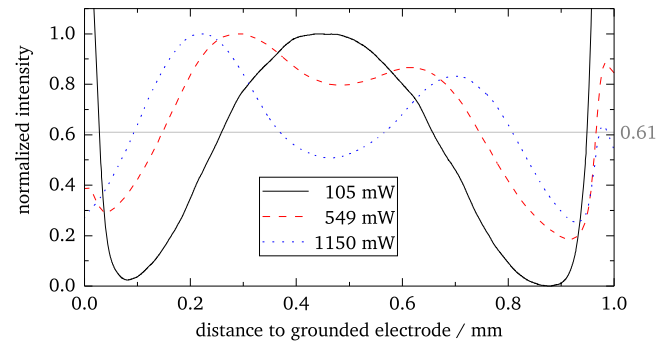
These spatial structures are particularly visible in the profiles extracted from the images by integrating over the horizontal axis (see figure 10). Here, the profiles were normalized to the intensity maximum in order to better demonstrate the spatial structure. The maxima at position 0 and 1 mm are due to reflections of the plasma at the electrode edges. The sheath width was then extracted from these profiles. In first approximation, the intensity is proportional to the electron density when the electron temperature can be assumed to be constant. In order to justify this assumption, the electron temperature was determined with the help of a Boltzmann solver. In the parameter range investigated here, only a minimal change in the electron temperature could be detected. For a collisionless ionization-free sheath, an ion density drop at the sheath edge to $\exp(-1/2)$ of the original bulk density follows from ion flux conservation, Bohm velocity and Boltzmann equation [39]. Therefore, as sheath edge criterion, a drop in intensity to $\exp(-1/2) \approx 0.61$ was assumed here. This value is marked in figure 10 by a gray horizontal line. The result is also shown in figure 8 represented by open red squares.

The development of the sheath width determined from the images as a function of the dissipated power corresponds exactly to the trends that were derived from the dissipated power using the global model. Only the absolute value differs considerably from the values in the model. However, this absolute value is strongly dependent on the selected definition for the sheath edge. Neither the factor 1 in the global model (see equation (9)) nor the drop to $\exp(-1/2)$ of the emission intensity represents a strong criterion. Further adaptations could be made here. Nevertheless, the empirical determination of the sheath width trend thus confirms the values determined from the electrical characteristic data, indicates that the systematic error for the sheath width is overestimated and thus justifies the use of the global model.

In summary, the sheath width in the helium discharge could be determined from the circuit model to around 250 μm. With increasing dissipated power the sheath width decreases. The absolute values as well as the relative trend are supported by the available literature. The experimental observation of the sheath width in the optical images also supports the observed trends.

3.2.2. Electron density. Electron density is one of the most important plasma parameters because it determines the Debye length, the plasma frequency, the electrical conductivity and the probability of electron-induced processes such as excitation or chemical reactions. The mean electron density can be estimated from the bulk plasma resistance R_b using impedance measurement and the homogeneous model [39]:

$$R_b = \frac{l - 2s_0}{A}\rho_b = \frac{l - 2s_0}{A}\frac{1}{\omega \, \text{Im}(\epsilon_p)}$$

$$= \frac{l - 2s_0}{A}\frac{\nu_m m_e}{e^2 n_e} \tag{10}$$

$$\Rightarrow n_e = \frac{l - 2s_0}{A R_b}\frac{\nu_m m_e}{e^2}. \tag{11}$$

Here, l denotes the interelectrode distance (1 mm for the COST-Jet) and ρ_b the bulk plasma resistivity. The electron-neutral collision frequency for helium at atmospheric pressure is $\nu_m = 1052 \times 10^{12}\,\text{s}^{-1}$ [54]. As mentioned before, in the parameter range investigated here, only a minimal change in the electron temperature could be detected. Therefore, we consider the assumption of a fixed collision frequency to be justified.

The reliability of the results of equation (11) depends strongly on the precision of the plasma impedance measurements but also on the validity of the circuit model used and thus on the operation mode of the plasma. Strictly speaking, the equivalent circuit diagram used here is not valid in γ-like mode, since it does not include power dissipation in the sheaths.

Figure 11 shows the electron density of a helium discharge as a function of the dissipated power. As expected, the electron density increases with dissipated power and is in the range of 4×10^{16}–$11 \times 10^{16}\,\text{m}^{-3}$.

The displayed error bar of the first electrical measurement data point represents the largest statistical error in the measurement which was 21.7%. The systematic errors are between 86% and 860% for the electron density. For comparison, Waskoenig's model [40] is again used, which predicts an electron density of $n_e = 12 \times 10^{16}\,\text{m}^{-3}$. This electron density (marked by a cross in figure 11) is only slightly above the values determined from the electrical measurements. The order of magnitude of the electrical measurements is therefore very well confirmed by modeling results indicating an overestimation of the systematic error.

For low powers the electron density rises steeply and unexpectedly flattens from about 0.28 W. For the time being, there is no obvious physical reason for this trend change. One possible explanation is the validity range of the model used: strictly speaking, the assumptions of the homogeneous model are only valid in the α-mode of the discharge. However, the power curve in figure 2 also shows a peculiarity. After an initial linear increase, the dissipated power rises exponentially from about 0.28 W with increasing voltage, which can be interpreted as the onset of γ-like mode. As described above, this mode is characterized by increased secondary electron emission in the sheaths, especially by Penning or pooling reactions. Consequently, due to the lack of power dissipation
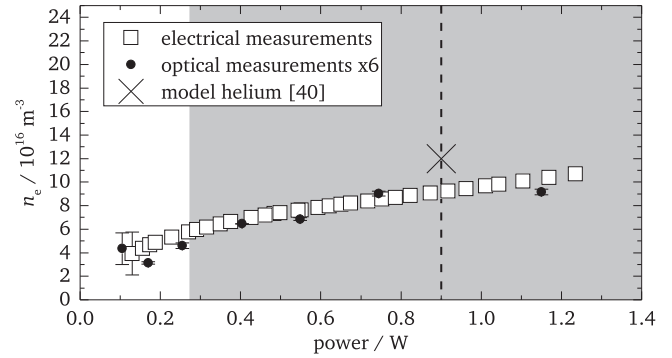
Figure 11. Electron density as function of dissipated power derived from electrical impedance (open squares) and optical measurements (filled circles) at a gas flow rate of 1000 sccm helium at atmospheric pressure. Note, that the values based on the optical measurements are multiplied here by a factor of 6. The dashed line and the cross mark modeling results from Waskoenig [40]. Gray area denotes limited applicability of the electrical model.

in the sheath model, the results should be considered with caution. For a complete description of this mode, additional sheath resistors representing the power dissipation by stochastic heating and a dc current source term for the generation of ions would have to be considered in the model [38]. However, due to these additional circuit elements, the mathematical problem would be undefined. The region of questionable validity of the model is shown in figure 11 with a gray background.

To check the validity in this operation mode, the electron density was additionally determined by optical emission spectroscopy using the method described in section 2.2. For this purpose a small amount of nitrogen was added to the pure helium discharge as tracer gas in order not to disturb the discharge. With the chosen admixture of 0.1 sccm only minimal changes in the helium spectrum of the discharge could be detected. The analysis of the emission spectra also yields an electron density which increases with increasing discharge power (see figure 11). The absolute values are a factor 6 below the densities calculated by impedance. One possible explanation is the different sensitivity of the methods to electron energies. Optical emission spectroscopy probes high energy electrons due to the required excitation energy. The electrical method probes mainly low energy electrons because their density is much higher. Small deviations in the electron energy distribution function can therefore cause a large difference in the electron density determined by the two methods. Notably, the error bars only represent the standard deviation of several measurements and do not reflect systematic errors due to the Boltzmann server and the rate equation model.

Considering the simplicity of the used electrical model and the uncertainties of the optical emission spectroscopy method, the agreement of the absolute values can be regarded as very good. Especially the relative trend with increasing voltage confirms the applicability of the homogeneous model in γ-like mode.

In summary, the electron density determined from the electrical model results in a value of some 10^{16} m^{-3}. As expected, the electron density increases with increasing dissipated power. The validity of the model was also confirmed in γ-like mode by an independent method based on optical emission spectroscopy.

4. Conclusion

In this publication we present the characterization of the COST-Jet using current, voltage and optical measurements. The built-in electrical probes allow *operando* measurement of dissipated power, the robustness of which has been demonstrated by detailed failure analysis. Three different measurement scenarios show that despite the small dimensions and the capacitive character of the discharge, a resilient *operando* measurement of the dissipated power is possible by carefully designing the probes and evaluating the electrical signal waveforms.

The implementation of an electrical equivalent circuit model for the discharge provides insight into fundamental plasma parameters. Thus, the contradiction between observed and expected plasma resistance can be resolved. The sheath width could be determined from the model to around 250 μm. With increasing power the sheath width decreases. This behavior can be confirmed by the extraction of the sheath width from optical images of the plasma emission. The electron density can also be determined from the bulk resistance. The result is between $4 \times 10^{16} - 11 \times 10^{16}$ m^{-3}. The electron density increases with increasing dissipated power. This behavior was additionally confirmed by an independent measurement via optical emission spectroscopy. Overall, the plasma parameters derived from the equivalent circuit diagram provide a coherent picture. The observations also agree very well with the experimental and numerical results from the already published literature.

All things considered, the measurement of the dissipated power allows an analysis of the energy consumed in the discharge. It can provide the answer to the fundamental question of how much energy is converted where in the system. The reliable measurement of absolute values allows the derivation of fundamental plasma parameters. Due to the *operando* character of the electrical measurements, real-time monitoring of the plasma parameters will also be possible in the future. This can be particularly interesting for applications in which plasmas are to be compared with different feed gases.

Acknowledgments

ORCID iDs

J Golda https://orcid.org/0000-0003-2344-2146
V Schulz-von der Gathen https://orcid.org/0000-0002-7182-3253

References

[1] Becker K H, Schoenbach K H and Eden J G 2006 Microplasmas and applications *J. Phys. D: Appl. Phys.* **39** R55–70

[2] Foest R, Schmidt M and Becker K 2006 Microplasmas, an emerging field of low-temperature plasma science and technology *Int. J. Mass Spectrom.* **248** 87–102

[3] Laroussi M and Akan T 2007 Arc-free atmospheric pressure cold plasma jets: a review *Plasma Process. Polym.* **4** 777–88

[4] Graves D, Hamaguchi S and O'Connell D 2015 In focus: plasma medicine *Biointerphases* **10** 029301

[5] Hirst A M, Frame F M, Arya M, Maitland N J and O'Connell D 2016 Low temperature plasmas as emerging cancer therapeutics: the state of play and thoughts for the future *Tumour Biol.* **37** 7021–31

[6] Coulombe S, Léveillé V, Yonson S and Leask R L 2006 Miniature atmospheric pressure glow discharge torch (APGD-t) for local biomedical applications *Pure Appl. Chem.* **78** 1147–56

[7] Foest R, Kindel E, Lange H, Ohl A, Stieber M and Weltmann K D 2007 RF capillary Jet—a tool for localized surface treatment *Contrib. Plasma Phys.* **47** 119–28

[8] Robert E, Barbosa E, Dozias S, Vandamme M, Cachoncinlle C, Viladrosa R and Pouvesle J M 2009 Experimental study of a compact nanosecond plasma gun *Plasma Process. Polym.* **6** 795–802

[9] Voráč J, Dvořák P, Procházka V, Ehlbeck J and Reuter S 2013 Measurement of hydroxyl radical (OH) concentration in an argon RF plasma jet by laser-induced fluorescence *Plasma Sources Sci. Technol.* **22** 025016

[10] Turner M M 2017 Computer simulation in low-temperature plasma physics: future challenges *Plasma Process. Polym.* **14** 1600121

[11] Begley C G and Ioannidis J P A 2015 Reproducibility in science: improving the standard for basic and preclinical research *Circ. Res.* **116** 116–26

[12] Baker M 2016 Is there a reproducibility crisis? *Nature* **533** 452–4

[13] Nature Editorial 2016 Reality check on reproducibility *Nature* **533** 437

[14] Knake N, Reuter S, Niemi K, Schulz-von der Gathen V and Winter J 2008 Absolute atomic oxygen density distributions in the effluent of a microscale atmospheric pressure plasma jet *J. Phys. D: Appl. Phys.* **41** 194006

[15] Bibinov N, Knake N, Bahre H, Awakowicz P and Schulz-von der Gathen V 2011 Spectroscopic characterization of an atmospheric pressure μ-jet plasma source *J. Phys. D: Appl. Phys.* **44** 345204

[16] Niermann B, Böke M, Sadeghi N and Winter J 2010 Space resolved density measurements of argon and helium metastable atoms in radio-frequency generated He-Ar microplasmas *Eur. Phys. J.* D **60** 489–95

[17] Lazovic S, Maletic D, Puac N, Malovic G, Dordevic A and Petrovic Z L 2010 Current-voltage characterstics of μ-APPJ obtained by using derivative probes *Proc. 20th ESCAMPIG (Novi Sad, Serbia, 13–17 July)*

[18] Miller P A, Anderson H and Splichal M P 1992 Electrical isolation of radio-frequency plasma discharges *J. Appl. Phys.* **71** 1171–6

[19] Ellerweg D, Benedikt J, von Keudell A, Knake N and Schulz-von der Gathen V 2010 Characterization of the effluent of a He/O$_2$ microscale atmospheric pressure plasma jet by quantitative molecular beam mass spectrometry *New J. Phys.* **12** 013021

[20] Jonkers J, van de Sande M, Sola A, Gamero A and van der Mullen J 2003 On the differences between ionizing helium and argon plasmas at atmospheric pressure *Plasma Sources Sci. Technol.* **12** 30–8

[21] Golda J *et al* 2016 Concepts and characteristics of the 'COST reference microplasma jet' *J. Phys. D: Appl. Phys.* **49** 084003

[22] Beijer P A C, Sobota A, van Veldhuizen E M and Kroesen G M W 2016 Multiplying probe for accurate power measurements on an RF driven atmospheric pressure plasma jet applied to the COST reference microplasma jet *J. Phys. D: Appl. Phys.* **49** 104001

[23] Offerhaus B, Lackmann J W, Kogelheide F, Bracht V, Smith R, Bibinov N, Stapelmann K and Awakowicz P 2017 Spatially resolved measurements of the physical plasma parameters and the chemical modifications in a twin surface dielectric barrier discharge for gas flow purification *Plasma Process. Polym.* **14** 1600255

[24] Bibinov N, Halfmann H, Awakowicz P and Wiesemann K 2007 Relative and absolute intensity calibrations of a modern broadband echelle spectrometer *Meas. Sci. Technol.* **18** 1327–37

[25] Pothiraja R, Ruhrmann C, Engelhardt M, Bibinov N and Awakowicz P 2013 Characterization of atmospheric-pressure ac micro-discharge in He–N$_2$ mixture using time- and space-resolved optical emission spectroscopy *J. Phys. D: Appl. Phys.* **46** 464012

[26] Dyatko N A, Kochetov I V, Napartovich A P and Sukharev A G 2011 EEDF: the software package for calculations of the electron energy distribution function in gas mixtures (https://fr.lxcat.net/download/EEDF/) (accessed 3 September 2019)

[27] Hopkins M RF matching network characterization: application note edited by Impedans Ltd (accessed 3 September 2019) (http://www.impedans.com/sites/default/files/pdf_downloads/rf_matching_unit_characterization.pdf)

[28] Golda J 2017 Cross-correlating discharge physics, excitation mechanisms and plasma chemistry to describe the stability of an RF-excited atmospheric pressure argon plasma jet *Dissertation* Ruhr-Universität Bochum, Bochum

[29] Xue J and Hopwood J A 2009 Microwave-frequency effects on microplasma *IEEE Trans. Plasma Sci.* **37** 816–22

[30] Iza F and Hopwood J 2005 Split-ring resonator microplasma: microwave model, plasma impedance and power efficiency *Plasma Sources Sci. Technol.* **14** 397–406

[31] Zhu W C, Wang B R, Yao Z X and Pu Y K 2005 Discharge characteristics of an atmospheric pressure radio-frequency plasma jet *J. Phys. D: Appl. Phys.* **38** 1396–401

[32] Overzet L J, Jung D, Mandra M A, Goeckner M, Dufour T, Dussart R and Lefaucheux P 2010 RF impedance measurements of DC atmospheric micro-discharges *Eur. Phys. J.* D **60** 449–54

[33] McKay K, Iza F and Kong M G 2010 Excitation frequency effects on atmospheric pressure helium RF microplasmas: plasma density, electron energy and plasma impedance *Eur. Phys. J.* D **60** 497–503

[34] Godyak V A, Piejak R B and Alexandrovich B M 1991 Electrical characteristics of parallel-plate RF discharges in argon *IEEE Trans. Plasma Sci.* **19** 660–76

[35] Marinov D and Braithwaite N S J 2014 Power coupling and electrical characterization of a radio-frequency micro atmospheric pressure plasma jet *Plasma Sources Sci. Technol.* **23** 062005

[36] Schröder D, Burhenn S, Kirchheim D and Gathen V S V D 2013 Enhanced oxygen dissociation in a propagating constricted discharge formed in a self-pulsing atmospheric pressure microplasma jet *J. Phys. D: Appl. Phys.* **46** 464003

[37] Spiekermeier S, Schröder D, Schulz-von der Gathen V, Böke M and Winter J 2015 Helium metastable density evolution in a self-pulsing μ-APPJ *J. Phys. D: Appl. Phys.* **48** 035203

[38] Lieberman M A and Lichtenberg A J 2005 *Principles of Plasma Discharges and Materials Processing* 2nd edn (Hoboken, NJ: Wiley-Interscience)

[39] Chabert P and Braithwaite N 2011 *Physics of Radio-Frequency Plasmas* (Cambridge and New York: Cambridge University Press)

[40] Waskoenig J 2010 Numerical simulations of the electron dynamics in single and dual radio-frequency driven atmospheric pressure plasmas and associated plasma chemistry in electro-negative He–O$_2$ mixtures *PhD Thesis* Queen's University Belfast, Belfast

[41] Raizer Y P, Shneider M N and Yatsenko N A 1995 *Radio-Frequency Capacitive Discharges* (Boca Raton, FL: CRC Press)

[42] Moravej M, Yang X, Nowling G R, Chang J P, Hicks R F and Babayan S E 2004 Physics of high-pressure helium and argon radio-frequency plasmas *J. Appl. Phys.* **96** 7011

[43] Moon S Y, Rhee J K, Kim D B and Choe W 2006 α, γ and normal, abnormal glow discharge modes in radio-frequency capacitively coupled discharges at atmospheric pressure *Phys. Plasmas* **13** 033502

[44] Shi J J and Kong M G 2006 Evolution of discharge structure in capacitive radiofrequency atmospheric microplasmas *Phys. Rev. Lett.* **96** 105009

[45] Kawamura E, Lieberman M A, Lichtenberg A J, Chabert P and Lazzaroni C 2014 Particle-in-cell and global simulations of α to γ transition in atmospheric pressure Penning-dominated capacitive discharges *Plasma Sources Sci. Technol.* **23** 035014

[46] Lazzaroni C, Chabert P, Lieberman M A, Lichtenberg A J and Leblanc A 2012 Analytical-numerical global model of atmospheric-pressure radio-frequency capacitive discharges *Plasma Sources Sci. Technol.* **21** 035013

[47] Schaper L, Waskoenig J, Kong M G, Schulz-von der Gathen V and Gans T 2011 Electron dynamics in a radio-frequency-driven microatmospheric pressure plasma jet *IEEE Trans. Plasma Sci.* **39** 2370–1

[48] Lieberman M A 1989 Dynamics of a collisional, capacitive RF sheath *IEEE Trans. Plasma Sci.* **17** 338–41

[49] Liu D W, Iza F and Kong M G 2008 Electron heating in radio-frequency capacitively coupled atmospheric-pressure plasmas *Appl. Phys. Lett.* **93** 261503

[50] Waskoenig J, Niemi K, Knake N, Graham L M, Reuter S, Schulz-von der Gathen V and Gans T 2010 Atomic oxygen formation in a radio-frequency driven micro-atmospheric pressure plasma jet *Plasma Sources Sci. Technol.* **19** 045018

[51] Hemke T, Eremin D, Mussenbrock T, Derzsi A, Donkó Z, Dittmann K, Meichsner J and Schulze J 2013 Ionization by bulk heating of electrons in capacitive radio frequency atmospheric pressure microplasmas *Plasma Sources Sci. Technol.* **22** 015012

[52] Bischoff L *et al* 2018 Experimental and computational investigations of electron dynamics in micro atmospheric pressure radio-frequency plasma jets operated in He/N$_2$ mixtures *Plasma Sources Sci. Technol.* **27** 125009

[53] Gibson A R *et al* 2019 Disrupting the spatio-temporal symmetry of the electron dynamics in atmospheric pressure plasmas by voltage waveform tailoring *Plasma Sources Sci. Technol.* **28** 01LT01

[54] Raizer Y P 1991 *Gas Discharge Physics* (Berlin, New York: Springer)